Constraints on the growth rate using the observed galaxy power spectrum

José Fonseca,[1,2,3] **Jan-Albert Viljoen,**[3] **Roy Maartens** [3,4]

[1]Dipartimento di Fisica e Astronomia "G. Galilei", Università degli Studi di Padova, Via Marzolo 8, 35131 Padova, Italy

[2]INFN, Sezione di Padova, via Marzolo 8, I-35131, Padova, Italy

[3]Department of Physics & Astronomy, University of the Western Cape, Cape Town 7535,
South Africa

[4]Institute of Cosmology & Gravitation, University of Portsmouth, Portsmouth PO1 3FX,

UK

E-mail: josecarlos.s.fonseca@gmail.com

Abstract. The large-scale structure growth index γ provides a consistency test of the standard cosmology and is a potential indicator of modified gravity. We investigate the constraints on γ from next-generation spectroscopic surveys, using the power spectrum that is observed in redshift space, i.e., the angular power spectrum. The angular power spectrum avoids the need for an Alcock-Packzynski correction. It also naturally incorporates cosmic evolution and wide-angle effects, without any approximation. We include the cross-correlations between redshift bins, using a hybrid approximation when the total number of bins is computationally unfeasible. We show that the signal-to-noise on γ increases as the redshift bin-width is decreased. Noise per bin also increases – but this is compensated by the increased number of auto- and cross-spectra. In our forecasts, we marginalise over the amplitude of primordial fluctuations and other standard cosmological parameters, including the dark energy equation of state parameter, as well as the clustering bias. Neglecting cross-bin correlations increases the errors by $\sim 40 - 150\%$. Using only linear scales, we find that a DESI-like BGS survey and an HI intensity mapping survey with the SKA1 precursor MeerKAT deliver similar errors of $\sim 4 - 6\%$, while a Euclid-like survey and an SKA1 intensity mapping survey give $\sim 3\%$ errors.

Contents

1 Introduction

We are entering a new era in the study of the large-scale structure (LSS) of the Universe. Not only will we map the sky over larger areas, but we will also go deeper in redshift. As well as the increasing volumes, we will probe the sky in different frequency ranges, creating complementary sets of dark matter tracers.

Einstein's theory of gravity and its modifications (see e.g. the reviews [1–3]) leave distinctive imprints on the clustering of matter and its peculiar velocity. Identifying the statistical effect of peculiar velocities on the distribution of matter provides a powerful test of the cosmological model and the theory of gravity. This test is based on using redshift-space distortions (RSD) to measure the LSS growth rate f or growth index $\gamma = \ln f / \ln \Omega_{\mathrm{m}}$. To implement this test one requires the redshift accuracy of spectroscopic surveys. Upcoming spectroscopic surveys, in optical, near infra-red and in radio bands [4–12], will have higher redshift accuracy and cover larger sky areas than ever, allowing for higher precision tests.

The standard analysis of RSD data for tests of gravity uses the spatial power spectrum $P_g(\boldsymbol{k}, z)$ in Fourier space, which allows one to cleanly separate the RSD effect via a Legendre multipole expansion (see e.g. [13] for the current state of the art). Similarly, most forecasts for future surveys rely on the same analysis (e.g. [14–16]). The Fourier power spectrum requires a choice of fiducial model to convert observed angles and redshifts to distances. This then requires an Alcock-Paczynski correction to compensate for the error in the choice of fiducial. In addition, the standard Fourier analysis implicitly neglects cosmic evolution in the rather thick redshift bins used, and it encodes a flat-sky approximation that neglects wide-angle correlations. There are prescriptions to deal with these issues (e.g. [17]). However, it

is useful to explore an alternative analysis that avoids these issues from the start (while of course introducing other issues).

The alternative is to use the angular power spectrum $C_\ell(z, z')$, which is the harmonic transform of the correlation function that is observed in redshift space – i.e., on the backward light-cone of the observer [18–22]. The angular power spectrum of the observed data does not require a fiducial model and therefore does not need an Alcock-Paczynski correction. Furthermore, it naturally incorporates wide-angle correlations and cosmic evolution. It also naturally incorporates Doppler and lensing magnification effects on the correlations, which we include, as well as other smaller relativistic observational effects, which we neglect here.

An immediate issue with $C_\ell(z, z')$ is that, unlike $P_g(\boldsymbol{k}, z)$, we cannot cleanly separate out the RSD effect. In addition, computational complexity arises from the oscillating spherical Bessel functions in $C_\ell(z, z')$, from cross-bin correlations for $z' \neq z$, and from the need for very thin redshift bins to maximally exploit the potential of spectroscopic surveys. Nevertheless, advances in using the angular power spectrum to analyse galaxy survey data are ongoing (e.g. [23–31]).

It is intuitively clear that thick redshift bins in C_ℓ will wash out the RSD signal so that thin bins are needed for precision on RSD. As redshift bins are decreased in size, the problem of noise grows, so that one might expect to reach a 'sweet spot' in bin width where the precision is optimal. This expectation is however not correct, since it ignores the additional information that arises from the growing number of auto- and cross-correlations. We confirm that information on the growth index γ continues to increase with decreasing bin width, reaching a theoretical maximum for infinitely thin bins. In practice we need to choose a bin width that is feasible for numerical computation.

We use Fisher forecasting and marginalise over the standard cosmological parameters, in particular including the amplitude of primordial fluctuations and the dark energy equation of state parameter, as well as over the clustering bias in each bin. Modelling nonlinear RSD is beyond the scope of this work and therefore we use information only from linear scales.

We find that the errors on γ for a Euclid-like survey and an SKA1 neutral hydrogen (HI) intensity mapping survey are $\sim 3\%$. We also find that an HI intensity mapping survey with the SKA1 precursor MeerKAT and a DESI-like BGS survey have a similar accuracy of $\sim 5\%$. Percent-level errors seem to be only within reach for the futuristic SKA2 HI galaxy survey. We also show that if only auto-correlations $C_\ell(z, z)$ are used and cross-bin correlations $C_\ell(z, z')$ are neglected, then the constraints degrade by a factor of $\sim 40 - 150\%$.

This paper is structured as follows. In §2 we review the effect of peculiar velocities in the angular power spectrum. §3 describes the technical assumptions on the surveys and tracers that we consider. In §4.1 we analyse the effect of redshift binning on RSD precision. Our results are presented in §4.2, and we conclude in §5. Our fiducial model is a concordance LCDM model with the Planck 2018 best-fit parameters.

2 Constraining the growth rate using the angular power spectrum

On linear scales, peculiar velocities are sourced by matter density gradients via the continuity equation,

$$\nabla \cdot \boldsymbol{v} = f\mathcal{H}\,\delta^{\mathrm{c}}\,, \tag{2.1}$$

where $\mathcal{H} = (\ln a)'$ is the conformal Hubble rate and δ^c is the comoving matter density contrast. The growth rate is

$$f \equiv \frac{\partial \ln D}{\partial \ln a}\,, \tag{2.2}$$

where D is the growth factor. The growth rate at any redshift z is clearly affected by the relative amount of dark matter at z, and we can alternatively use the growth index γ, defined by

$$f = \left(\Omega_{\mathrm{m}}\right)^{\gamma}\,. \tag{2.3}$$

For the standard LCDM model, $\Omega_{\mathrm{m}} = \Omega_{\mathrm{m0}}(1+z)^3[\Omega_{\mathrm{m0}}(1+z)^3 + 1 - \Omega_{\mathrm{m0}}]^{-1}$, and $\gamma = 0.545$ is a very good approximation. This approximation remains good for simple models of dynamical dark energy. For modified gravity models, the approximation breaks down and γ is significantly different. Hence measuring the growth index (or the growth rate) provides a test of LCDM and potentially of General Relativity. Note that f and γ are scale-independent in LCDM (and to a good approximation in simple extensions of LCDM), and the redshift dependence of f is determined by Ω_{m}. In modified gravity models there is typically scale dependence in f and thus in γ, and γ will also be redshift dependent. Here our focus is on a new approach to growth constraints via the angular power spectrum and we assume constant γ, which applies to LCDM and wCDM, the simple extension that we consider.

The number of sources counted by the observer in a solid angle element about unit direction $\boldsymbol{n}$ and in a redshift interval is given by

$$\mathrm{d}\mathbb{N} = N\mathrm{d}z\,\mathrm{d}\Omega_{\boldsymbol{n}} = \mathcal{N}\,\mathrm{d}V\,. \tag{2.4}$$

Here N is the number that is counted by the observer per redshift per solid angle. By contrast, $\mathcal{N}$ is the proper number density, which is not observed by the observer but is the quantity that would be measured at the source. Similarly, $\mathrm{d}V$ is not the observed volume element but the proper volume element corresponding to $\mathrm{d}z$ and $\mathrm{d}\Omega_{\boldsymbol{n}}$, as measured at the source. Then the observed number density contrast is δ_N, which is related to the proper number density contrast at the source as

$$\delta_N = \delta_{\mathcal{N}} + \mathrm{RSD} + \mathrm{Doppler} + \mathrm{lensing\ corrections}$$
$$= \delta_{\mathcal{N}} - \frac{1}{\mathcal{H}}\boldsymbol{n}\cdot\nabla\left(\boldsymbol{v}\cdot\boldsymbol{n}\right) + A\left(\boldsymbol{v}\cdot\boldsymbol{n}\right) + (2-5s)\kappa\,, \tag{2.5}$$

where A and κ are given in harmonic space in (2.10) below and s is given in (2.13). The observed two-point correlation function then defines the angular power spectrum:

$$\left\langle \delta_N(z_i,\boldsymbol{n})\,\delta_N(z_j,\boldsymbol{n}')\right\rangle = \sum_{\ell} \frac{(2\ell+1)}{4\pi}\,C_\ell(z_i,z_j)\,\mathcal{L}_\ell\left(\boldsymbol{n}\cdot\boldsymbol{n}'\right)\,, \tag{2.6}$$

where $\mathcal{L}_\ell$ are Legendre polynomials.

The number density contrast observed on the backward light-cone can be given directly in terms of the fundamental observables z_i and $\boldsymbol{n}$ by expanding in spherical harmonics:

$$\delta_N(z_i,\boldsymbol{n}) = \sum_{\ell m} a_{\ell m}(z_i)\,Y_{\ell m}(\boldsymbol{n})\,. \tag{2.7}$$

For now we assume that the redshift bin is an infinitesimal shell centred at z_i, and then we treat the realistic case below. By statistical homogeneity and isotropy, $\langle a_{\ell m}\rangle = 0$, and we can use the $a_{\ell m}$ and their covariance as estimators of the cosmological parameters. We assume that the $a_{\ell m}$ are Gaussian distributed with covariance

$$\left\langle a_{\ell m}(z_i)\,a^*_{\ell'm'}(z_j)\right\rangle = \delta_{\ell\ell'}\,\delta_{mm'}\,C_\ell(z_i,z_j)\,. \tag{2.8}$$

2.1 Angular transfer functions

We follow the notation and approach of [18] and relate the covariance of the $a_{\ell m}$ with the primordial power spectrum of the curvature perturbation $\mathcal{P}(k)$ and the theoretical transfer functions Δ_ℓ as

$$C_\ell(z_i, z_j) = 4\pi \int \mathrm{d}\ln k \, \Delta_\ell(z_i, k) \, \Delta_\ell(z_j, k) \, \mathcal{P}(k). \tag{2.9}$$

The primordial power spectrum $\mathcal{P}(k) = A_s (k/k_0)^{n_s-1}$ encodes information about the seeds of structure formation via its amplitude A_s and spectral index n_s. The pivot scale is set to $k_0 = 0.05\,\mathrm{Mpc}^{-1}$. The transfer functions include the tracer density contrast, as well as RSD and all other observational effects on the 2-point correlation function. In this paper we focus on the effects from peculiar velocities (RSD and the Doppler effect) and also include the effect of lensing magnification. Further effects are suppressed by a factor $\mathcal{H}^2/k^2$ and we neglect them. (The full expression can be found in [18–20, 32] for galaxy surveys and in [33, 38] for maps of intensity.) Then the theoretical transfer function is given by

$$\begin{aligned}
\Delta_\ell(k) = {}& b\, \delta_k^{\mathrm{c}}\, j_\ell(k\chi) + \frac{k v_k}{\mathcal{H}} j_\ell''(k\chi) \\
& + \left(\frac{2 - 5s}{\mathcal{H}\chi} + 5s - b_e + \frac{\mathcal{H}'}{\mathcal{H}^2} \right) v_k j_\ell'(k\chi) \\
& + \frac{\ell(\ell+1)(2-5s)}{2} \int_0^\chi \mathrm{d}\tilde{\chi} \frac{(\chi - \tilde{\chi})}{\chi \tilde{\chi}} \left[\phi_k(\tilde{\chi}) + \psi_k(\tilde{\chi}) \right] j_\ell(k\tilde{\chi}),
\end{aligned} \tag{2.10}$$

where we suppressed the redshift dependence to simplify notation. The first line corresponds to the standard density plus RSD terms, the second line is the Doppler term and the third line the lensing contribution. Here χ is the comoving line-of-sight distance, j_ℓ are spherical Bessel functions and the perturbed metric is given in Poisson gauge by

$$\mathrm{d}s^2 = a^2 \left[-\left(1 + 2\psi\right)\mathrm{d}\eta^2 + \left(1 - 2\phi\right)\mathrm{d}\boldsymbol{x}^2 \right]. \tag{2.11}$$

In addition to the clustering bias b in (2.10), we also have the 'evolution bias', accounting for redshift evolution of sources, and the magnification bias, accounting for the way that lensing alters the number of sources that actually enter in the survey:

$$b_e = \frac{\partial \ln a^3 \bar{\mathcal{N}}}{\partial \ln a}, \tag{2.12}$$

$$s = \frac{\partial \log_{10} \bar{\mathcal{N}}}{\partial m_*}. \tag{2.13}$$

Here m_* is the threshold magnitude of the survey and the background number density of sources is $\bar{\mathcal{N}} = \bar{\mathcal{N}}(z, m < m_*)$. In the background, $\bar{N} = \bar{\mathcal{N}}\chi^2(1+z)^{-4}\mathcal{H}^{-1}$. (From now on we drop the overbar on the background values of $\mathcal{N}, N, \mathbb{N}$.)

So far we assumed that the survey window function is given by a delta function. In reality, the observed transfer function $\Delta_\ell^W(z_i, k)$ includes the fact that the window function W may weight different redshifts differently and that the redshift distribution of sources p may not be constant in redshift:

$$\Delta_\ell^W(z_i, k) = \int \mathrm{d}z \, p(z) \, W(z_i, z) \, \Delta_\ell(z, k). \tag{2.14}$$

Hence p and W work as redshift weighting functions of the theoretical transfer function. Note that the product pW is thus normalised to unity for galaxy surveys: $\int dz\, p(z)W(z_i, z) = 1$ for all z_i. In fact $p \propto N = d\mathbb{N}/(dz d\Omega)$, the (background) observed number density per z per Ω for galaxy surveys (see below for the case of intensity mapping) so we will present the window function in the next sections leaving all normalisations included in p.

2.2 Fisher matrix analysis

We write the Fisher matrix for a set of parameters ϑ_α as [34]

$$F_{\vartheta_\alpha \vartheta_\beta} = \sum_{\ell_{\min}}^{\ell_{\max}} \frac{(2\ell + 1)}{2} f_{\text{sky}} \operatorname{Tr}\left[(\partial_{\vartheta_\alpha} C_\ell) \Gamma_\ell^{-1} (\partial_{\vartheta_\beta} C_\ell) \Gamma_\ell^{-1} \right], \tag{2.15}$$

where C_ℓ is the matrix $C_\ell^{ij} = C_\ell(z_i, z_j)$. The survey sky fraction $f_{\text{sky}} = \Omega_{\text{survey}}/4\pi$ is an approximation accounting for the m summation. For simplicity we have not binned in ℓ. The observed covariance includes the noise term, $\Gamma_\ell = C_\ell + \text{Noise}_\ell$, and we assume that the noise terms do not depend on the cosmological parameters. In practice one uses C_ℓ and its covariance (see [21] for details) as the observable at high ℓ where we can safely assume that its likelihood is Gaussian and the $a_{\ell m}$ only at low ℓ where it is computationally feasible. For Fisher forecasts, the two approaches are equivalent.

The lower limit of the sum in (2.15) is the largest angular scale in the survey. If a survey covers a single spherical cap, then the maximum angular scale available is given by the survey area, i.e.,

$$\ell_{\min} = \operatorname{int}\left(\pi/\sqrt{\Omega_{\text{survey}}} \right) + 1. \tag{2.16}$$

To allow for more realistic sky coverage, we use a smaller $\ell_{\min}$. Furthermore, in the case of HI intensity mapping, the removal of foregrounds affects the largest scales, $\ell_{\min} \lesssim 5$ [35, 36]. We impose $\ell_{\min} = 5$ in all surveys. Scales with $\ell_{\min} < 5$ will contribute negligibly to constraints on the growth rate.

Under the assumption that the $a_{\ell m}$ likelihood is Gaussian, the inverse of the Fisher matrix is a good approximation of the parameter covariance. Hence the forecasted marginal and conditional errors for a parameter ϑ_α are given by

$$\sigma_{\vartheta_\alpha} = \left[(F^{-1})_{\vartheta_\alpha \vartheta_\alpha} \right]^{1/2}, \qquad \sigma_{\vartheta_\alpha}^{\text{cond}} = (F_{\vartheta_\alpha \vartheta_\alpha})^{-1/2}. \tag{2.17}$$

We consider the following set of parameters:

$$\vartheta_\alpha = \left\{ \ln \gamma, \ln A_s, b(z_i), \ln n_s, \ln \Omega_{\text{cdm0}}, \ln \Omega_{\text{b0}}, w, \ln H_0 \right\}. \tag{2.18}$$

For the cosmological parameters we use the fiducial values: $A_s = 2.142 \times 10^{-9}$, $n_s = 0.967$, $\Omega_{\text{cdm0}} = 0.26$, $\Omega_{\text{b0}} = 0.05$, $w = -1$, $H_0 = 67.74$ km/s/Mpc. For the growth index, we take $\gamma = 0.545$, as discussed above. In addition, the clustering bias in each bin, $b(z_i)$, is a free parameter, with fiducial value set by the bias models for each survey (see §3). We assumed Gaussian priors from Planck 2018 [37] for all cosmological parameters. The priors are on the parameters, not their logarithms; we use the log of the parameters in the Fisher matrix purely because this gives a numerically more stable inversion of the matrix (see [27] for more detail).

The number of bias parameters is survey- and binning-dependent and is discussed in §3. As will become clear, in some experiments the number of bins introduces computational limitations, and we develop a means to deal with this, following the idea proposed in [27].

The angular power spectra and their derivatives are computed using CAMB_sources. The derivatives with respect to $\ln\Omega_{cdm0}, \ln\Omega_{b0}, w, \ln H_0$ are taken numerically using the 5-point stencil method. For the remaining parameters, we use a modified CAMB_sources to accept analytical derivatives.[1] The analytical derivative with respect to γ uses the parametrisation (2.3), so that $\partial f/\partial\gamma = f\ln\Omega_m$. Then

$$\frac{\partial}{\partial\gamma}C_\ell(z_i, z_j) = \int d\ln k \left[\Delta_\ell^W(z_j) \int dz'\, p(z')\, W(z', z_i)\, \ln\Omega_m\, \Delta_\ell^{\boldsymbol{v}} \right.$$
$$\left. + \Delta_\ell^W(z_i) \int dz''\, p(z'')\, W(z'', z_j)\, \ln\Omega_m\, \Delta_\ell^{\boldsymbol{v}} \right] \mathcal{P}(k), \qquad (2.19)$$

where $\Delta_\ell^{\boldsymbol{v}}$ denotes the RSD and Doppler terms in (2.10). The analytical derivatives with respect to A_s, n_s and the biases are given in Appendix A of [38].
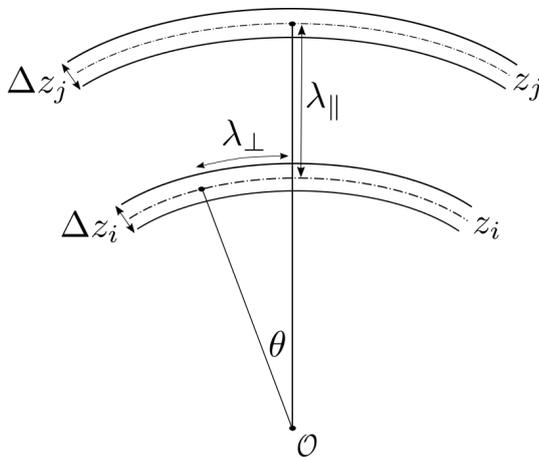
2.3 Excluding nonlinear effects

Figure 1. Scales associated with a multipole ℓ.

When computing forecasts we only consider linear perturbations. The inclusion of nonlinear effects is beyond the scope of this paper and we therefore need to choose ℓ_{max} in (2.15) to exclude these effects from the Fisher matrix. In Fourier space, the scale marking the breakdown of a perturbative analysis of matter clustering is given in [39] as

$$k_{nl}(z) = k_{nl,0}\,(1+z)^{2/(2+n_s)} \quad \text{with} \quad k_{nl,0} \simeq 0.2h\,\text{Mpc}^{-1}. \qquad (2.20)$$

On the scales of interest, the multipole ℓ corresponds to a transverse comoving length scale $\lambda_\perp = 2\pi/k$, which subtends an angle $\theta = \lambda_\perp/\chi$ at the observer (see Figure 1). Using $\theta = 2\pi/\ell$, this gives $\ell = \chi k$. It follows that, for auto-correlations, the maximum multipole is

$$\ell_{max}(z_i, z_i) = \chi(z_i)k_{nl}(z_i). \qquad (2.21)$$

The case of cross-bin correlations is more complicated (see the discussion in [21]). In principle, one can allow for $\ell \gg 1$ in the case of near-radial correlations, for which $\theta \ll 1$ and $\lambda_\perp \ll 2\pi/k_{nl}$ – provided that $\lambda_\parallel > 2\pi/k_{nl}$, to ensure that $\lambda > 2\pi/k_{nl}$. However, in order

---

[1] https://github.com/ZeFon/CAMB_sources_MT_ZF.git

to fully exclude nonlinearities from the Fisher matrix, we need to exclude them also from the covariance of C_ℓ^{ij}, which contains the term $C_\ell^{ii} C_\ell^{jj}$. If $\lambda_\perp$ is nonlinear then C_ℓ^{ii} includes nonlinear effects and hence the covariance contains nonlinearities. Therefore we impose the cut

$$\ell_{\max}(z_i, z_j) = \min\{\ell_{\max}(z_i, z_i), \ell_{\max}(z_j, z_j)\}. \tag{2.22}$$

3 Future spectroscopic surveys

To access the information encoded in the velocity field one requires the high redshift resolution of spectroscopic galaxy count surveys or intensity mapping (IM) surveys. We focus only on HI IM; in the future other line IM surveys may be available.

In galaxy surveys the main source of uncertainty is the shot noise:

$$\mathcal{S}_\ell^g(z_i, z_j) = \frac{1}{N_\Omega(z_i)}\,\delta_{ij}\,, \tag{3.1}$$

where the average angular density of sources in the bin is

$$N_\Omega(z_i) = \int \mathrm{d}z\, W(z, z_i)\, N(z)\,. \tag{3.2}$$

For photometric galaxy surveys the window function is generically an error function [40], which one can extend to spectroscopic redshift surveys but with narrow redshift uncertainties. For spectroscopic surveys this error function window function becomes very close to a smooth top-hat, which is also numerically stable. We use the smoothed top-hat window:

$$W(z, z_i; \Delta z_i, \sigma_z) = \frac{1}{2 \tanh(\Delta z_i/2\sigma_{zi})} \left[\tanh\left(\frac{z - z_i + \Delta z_i/2}{\sigma_{zi}}\right) - \tanh\left(\frac{z - z_i - \Delta z_i/2}{\sigma_{zi}}\right) \right], \tag{3.3}$$

where σ_z is the redshift resolution and $\sigma_{zi} = \sigma_z(1 + z_i)$. This window function applies to both spectroscopic galaxy and IM surveys.

In the case of HI IM, the noise component is thermal, coming mainly from the instrument. For single-dish IM experiments, where the dish signals are simply added rather than combined interferometrically, the instrumental noise is similar to CMB experiments [41], and is given by

$$\mathcal{T}_\ell^{\mathrm{HI}}(z_i, z_j) = \frac{4\pi\, f_{\mathrm{sky}}\, T_{\mathrm{sys}}^2}{2\, N_{\mathrm{d}}\, \Delta\nu\, t_{\mathrm{tot}}}\,\delta_{ij}\,. \tag{3.4}$$

Here T_{sys} is the system temperature of the telescope (including contributions from the receiver and the sky), N_{d} is the number of dishes, $\Delta\nu$ is the band size and t_{tot} is the total integration time. The factor of 2 comes from the two polarisations.

The angular power spectrum C_ℓ^{HI} of the theoretically observed HI temperature fluctuations is modified by the effect of the telescope beam:

$$C_\ell^{\mathrm{HI}}(z_i, z_j) \;\to\; C_\ell^{\mathrm{beam,HI}}(z_i, z_j) = B_\ell(z_i)\, B_\ell(z_j)\, C_\ell^{\mathrm{HI}}(z_i, z_j)\,. \tag{3.5}$$

Assuming a Gaussian beam, we have

$$B_\ell = \exp\left[-\frac{\ell\,(\ell + 1)}{16 \ln 2}\,\theta_{\mathrm{res}}^2\right], \tag{3.6}$$

where the angular resolution of the dishes with diameter D_{d} is

$$\theta_{\mathrm{res}} = 1.22\,\frac{\lambda_{\mathrm{obs}}}{D_{\mathrm{d}}}\,\mathrm{rad}\,. \tag{3.7}$$

Table 1. SKA1 and MeerKAT: dish and receiver properties.

Receiver	Frequency range [MHz]	Redshift range	Dish size [m]	# dishes
Band 1	$350 - 1050$	0.35–3.06	15	133
Band 2	$950 - 1760$	0.1–0.49	15	133
UHF-band	$580 - 1015$	0.4–1.45	13.5	64
L-band	$900 - 1670$	0.1–0.58	13.5	64

3.1 HI intensity mapping surveys

Intensity mapping of the 21cm HI emission line (after reionization) integrates the total emission from all galaxies in a pixel, giving a map of fluctuations at each z, with extremely small redshift error. This includes the emission from the brightest galaxies as well as from otherwise undetectable faint objects. The properties of this tracer are survey independent, which is not the case for galaxy surveys. We follow [42] and use a halo-based model for the HI average temperature and clustering bias, with the fitting functions:

$$\bar{T}^{\mathrm{HI}}(z) = 0.056 + 0.232z - 0.024z^2 \,, \tag{3.8}$$

$$b_{\mathrm{IM}}^{\mathrm{HI}}(z) = 0.667 + 0.178z + 0.050z^2 \,. \tag{3.9}$$

There is no threshold magnitude for IM, but there is a simple relation between the observed brightness temperature and the observed number counts of 21cm emitters, which allows us to use the number count contrast formulas (2.5) and (2.10), with the IM clustering bias and the following evolution bias and *effective* magnification bias [33, 43]:

$$(b_e)_{\mathrm{IM}}^{\mathrm{HI}} = \frac{\partial \ln \left[\bar{T}^{\mathrm{HI}}\mathcal{H}\right]}{\partial \ln a} - 3\,, \qquad \left(s_{\mathrm{IM}}^{\mathrm{HI}}\right)_{\mathrm{eff}} = \frac{2}{5}\,. \tag{3.10}$$

Then we have

$$\delta_T = \delta_N \Big|_{b_e,s \text{ from (3.10)}}\,. \tag{3.11}$$

We consider HI IM surveys with[2] SKA1-Mid [12] and its precursor[3] MeerKAT [11]. MeerKAT is operational; its 64 dishes will eventually be incorporated into SKA1-Mid with 133 new dishes. Since MeerKAT will produce results earlier than SKA1, we consider it separately. The total dishes, times and sky areas for the surveys are as follows:

$$\text{SKA1 IM:} \quad N_{\mathrm{d}} = 197\,, \ t_{\mathrm{tot}} = 10{,}000\,\mathrm{hr}\,, \ \Omega = 20{,}000\,\mathrm{deg}^2\,,$$
$$\text{MeerKAT IM:} \quad N_{\mathrm{d}} = \ 64\,, \ t_{\mathrm{tot}} = 4{,}000\,\mathrm{hr}\,, \ \Omega = \ 4{,}000\,\mathrm{deg}^2\,.$$

Dish and receiver properties are shown in Table 1, where Band 1, 2 refer to the receivers of the 133 new dishes, while UHF- and L-bands refer to the receivers of the 64 MeerKAT dishes. We use the terms SKA1 IM1,2 and MeerKAT IM-U,L for the high- and low-redshift surveys. The different properties of the MeerKAT and new SKA dishes complicate the thermal noise and beam properties of SKA1 IM1,2. The details are given in Appendix A.

3.2 HI galaxy surveys

For HI IM we considered radio dish arrays in single-dish mode. On the other hand, they can also be used as interferometers, increasing their angular resolution to be able to detect individual radio galaxies. If the 21cm line is present then one can measure the redshift of the galaxy, with extremely high redshift precision: this is the radio equivalent of an optical spectroscopic survey, with the noise also given by (3.2).

We use the parametrisations of simulations of HI galaxies given in [44] for the redshift distribution and clustering bias:

$$N_g^{\mathrm{HI}} \equiv \frac{\mathrm{d}\mathbb{N}_g^{\mathrm{HI}}}{\mathrm{d}z\mathrm{d}\Omega} = 10^{c_1} z^{c_2} \exp\left(-c_3 z\right) \mathrm{gal/\deg^2},\tag{3.12}$$

$$b_g^{\mathrm{HI}} = c_4 \exp\left(c_5 z\right).\tag{3.13}$$

For the magnification bias we use the parametrisation from [45][4]:

$$s_g^{\mathrm{HI}}(z) = \frac{2}{5}\left[a_1(z) + 2a_2(z)\ln\frac{F_*}{\mu\mathrm{Jy}} + 3a_3(z)\left(\ln\frac{F_*}{\mu\mathrm{Jy}}\right)^2\right],\tag{3.14}$$

where F_* is the threshold flux corresponding to m_* in (2.13). The fit for the a_i parameterisations can be found in table A1 of [45] up to $z = 1.5$, but has been computed[5] up to $z = 3$. The evolution bias is computed directly inside CAMB_SOURCES using (2.12) and (3.12).

Table 2. Fitting coefficients of (3.12) and (3.13) for SKA HI galaxy surveys.

	c_1	c_2	c_3	c_4	c_5	F_*
SKA1 Gal	5.45	1.31	14.4	0.616	1.02	$100\mu\mathrm{Jy}$
SKA2 Gal	6.77	2.17	6.63	0.588	0.808	$5\mu\mathrm{Jy}$

We consider two HI galaxy surveys: the SKA1 Medium-Deep Band 2 Survey (hereafter SKA1 Gal) [12] and a more futuristic SKA2 Gal [46]:

$$\begin{aligned}
\text{SKA1 Gal:} \quad &\Omega = 5,000\,\mathrm{deg}^2, \quad 0.1 \leq z \leq 0.58, \quad F_* = 100\,\mu\mathrm{Jy}, \\
\text{SKA2 Gal:} \quad &\Omega = 25,000\,\mathrm{deg}^2, \quad 0.1 \leq z \leq 2.0, \quad F_* = 5\,\mu\mathrm{Jy}.
\end{aligned}$$

We assume that $F_* = 5\sigma$, where σ is the flux sensitivity. See Table 2 for the values of the fitting coefficients in (3.12) and (3.13) for these two surveys (using [44]).

3.3 Optical/near-infrared spectroscopic surveys

We consider one high- and one low-redshift future survey:

Euclid-like Hα galaxy survey

Euclid[6] is a space telescope with an NISP spectrometer in the near-infrared (NIR), $1100 - 2000\,\mathrm{nm}$. Using the Hα line to determine the redshift, this corresponds to $z = 0.68 - 2.04$.

---

[4]Erratum MNRAS 467, 1505 (2017).

[5]S. Camera, private communication.

[6]www.euclid-ec.org

Based on several datasets, [47] have presented fits for Hα luminosity functions as a function of redshift. From these results, and assuming that the flux threshold of an NISP-like spectrometer is $\sim 2 \times 10^{-16}$erg/s/cm^2, [27] find the following fits for the redshift distribution of spectroscopic Hα galaxies and their magnification bias:

$$N_g^{\mathrm{H}\alpha} \equiv \frac{\mathrm{d}\mathbb{N}_g^{\mathrm{H}\alpha}}{\mathrm{d}z\mathrm{d}\Omega} = z^{1.11} \exp\left(9.91 - 0.84z - 1.26z^2 + 0.40z^3 - 0.04z^4\right) \, \mathrm{gal}/\deg^2\,, \quad (3.15)$$

$$s_g^{\mathrm{H}\alpha} = 0.49 + 0.41z - 0.17z^2 + 0.05z^3 - 0.01z^4\,, \quad (3.16)$$

$$b_g^{\mathrm{H}\alpha} = \sqrt{1+z}\,. \quad (3.17)$$

The galaxy bias follows [15, 48]. CAMB_SOURCES directly computes the evolution bias using (2.12) and (3.15). We assume a sky area of $15,000 \deg^2$.

Table 3. Basic details of the surveys.

Experiment	Tracer	Sky area [$10^3 \deg^2$]	t_{tot} [10^3hr]	Redshift range	Spectral resolution
MeerKAT IM-L	HI IM	4	4	0.1–0.58	10^{-4}
MeerKAT IM-U	HI IM	4	4	0.4–1.45	10^{-4}
SKA1 IM2	HI IM	20	10	0.1–0.58	10^{-4}
SKA1 IM1	HI IM	20	10	0.35–3.06	10^{-4}
SKA1 Gal	HI galaxies	5	—	0.1–0.58	10^{-4}
SKA2 Gal	HI galaxies	25	—	0.1–2.0	10^{-4}
Euclid-like	Hα galaxies	15	—	0.68–2.05	10^{-3}
DESI-like	Bright galaxies	15	—	0.1–0.6	10^{-3}

DESI-like bright galaxy sample

The Dark Energy Spectroscopic Instrument (DESI)[7] is a ground-based experiment whose spectrometer will determine the redshift of millions of galaxies with a redshift resolution of around 1%. The survey will target, among others, Luminous Red Galaxies (LRG), Emission Line Galaxies (ELG), Quasars and a Bright Galaxy Sample (BGS) [49]. The BGS sample is at low redshifts ($z = 0.05 - 0.6$) while the others are at higher redshifts. Here we consider a DESI-like BGS survey only, as a low-redshift complement to a Euclid-like Hα survey – which on its own provides better constraints than the higher-redshift samples of a DESI-like survey.

We use the fits to simulations from [49] for the astrophysical properties of these galaxies:

$$N_g^{\mathrm{BGS}} \equiv \frac{\mathrm{d}\mathbb{N}_g^{\mathrm{BGS}}}{\mathrm{d}z\mathrm{d}\Omega} = 6.0 \times 10^3 \left(\frac{z}{0.28}\right)^{0.91} \exp\left[-\left(\frac{z}{0.28}\right)^{2.56}\right] \, \mathrm{gal}/\deg^2\,, \quad (3.18)$$

$$b_g^{\mathrm{BGS}} = 0.99 + 0.73z - 1.29z^2 + 10.21z^3\,. \quad (3.19)$$

The evolution bias is computed directly inside CAMB_SOURCES using (2.12) and (3.18). We neglect the lensing contribution to the angular power spectrum, which is a very good approximation for low-redshift spectroscopic surveys.

We summarise in Table 3 the basic observational details of the surveys considered.
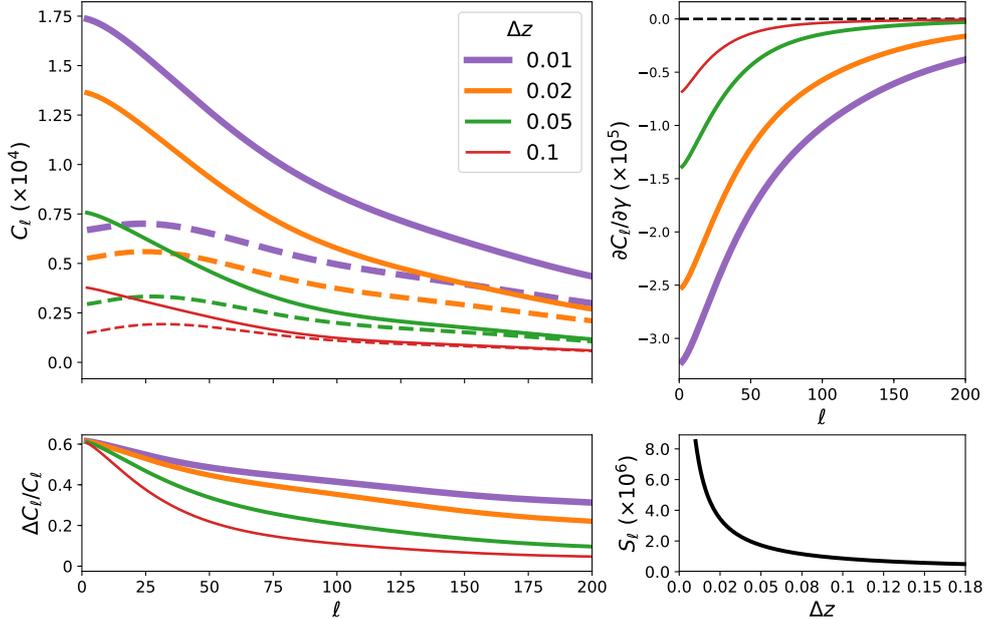
---

[7]www.desi.lbl.gov

Figure 2. For a Euclid-like survey, with different bin widths at $z_i = 1$. *Top left:* $C_\ell(z_i, z_i)$ without RSD (dashed) and with RSD (solid). *Bottom left:* fractional RSD contribution to total angular power, where $\Delta C_\ell = C_\ell(\text{total}) - C_\ell(\text{density only})$. *Top right:* Fisher derivative $\partial C_\ell / \partial \gamma$. *Bottom right:* shot noise (3.1).

4 Results

4.1 Redshift binning and the precision on RSD

In a Fisher analysis of the Fourier power spectrum $P_g(\boldsymbol{k})$, the redshift bin width does not affect the analysis, provided that Δz is not too large (typically $\Delta z \lesssim 0.1$ is chosen). The important binning in the Fourier case is in k-space. For the angular power spectrum C_ℓ, the Fisher analysis is different and the bin width is important for spectroscopic surveys. In this case, we need to apply redshift binning in a way that corresponds to the observable of interest. For example, if we choose broad redshift bins, then this will suppress the RSD signal, since peculiar motions will tend to average out. We can confirm this expectation by looking at the relative strength of RSD in the angular power spectrum as the bin width is decreased. A typical example is shown in Fig. 2 (top left), where we plot $C_\ell(z_i, z_i)$ without RSD (dashed) and with RSD (solid), for different bin widths Δz; the fractional RSD contribution is shown in the bottom left panel. The Fisher information on the growth rate index γ also increases with decreasing bin width, as shown in the top right plot.

It is clear from these plots that one can in principle extract more information from RSD by decreasing the width of the redshift bin. On the other hand, this also increases the shot noise (3.1), since $N_\Omega \sim N \Delta z$ (and similarly for the instrumental noise (3.4)). The increase in shot noise with decreasing bin width is illustrated in Fig. 2 (bottom right).

One might expect that the battle between increasing signal and growing noise produces a 'sweet spot' where information is maximised. The left panel of Fig. 3 appears to show
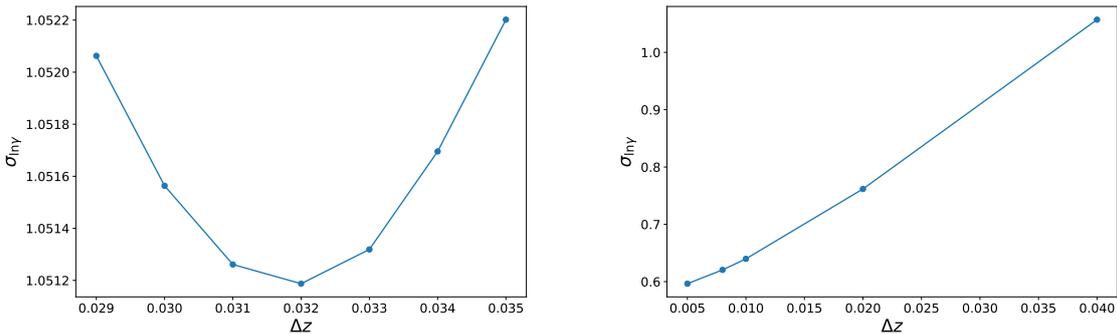
Figure 3. SKA1 IM1 survey centred at $z_i = 2$. Dependence of the conditional γ error on the redshift bin width: for a single bin of varying width (*left*); for a growing number of sub-divisions with fixed total size of 0.04, including all auto- and cross-correlations (*right*).

this, for a bin centred at redshift $z_i = 2$ in a SKA1 IM1 survey. We vary the width of a single redshift bin and find an optimal bin size that minimises the conditional error from auto-correlations. However, the problem with this apparent optimisation, is that we have neglected *cross-correlations*. Decreasing the bin width means an increase in the number of bins, and consequently an even greater increase in the number of auto- and cross-spectra amongst the redshift bins. The additional information from these correlations compensates for the increased noise per bin. This is illustrated in the right panel of Fig. 3. We fix the total redshift range to 0.04, subdivide it into bins 8 bins of $\Delta z = 0.005$, 5 bins of $\Delta z = 0.01$, 2 bins with $\Delta z = 0.02$ and a single bin with $\Delta z = 0.04$. Then we compute the conditional constraints on γ including cross-correlations between redshift bins. The 'sweet spot' at $\Delta z \sim 0.032$ in the left panel is not seen once the cross-correlations are included. Therefore we can in principle reduce the bin size down to the size of the receiver bands, which is $\sim 3 \times 10^{-4}$ at $z_i = 2$.

The implication is that we should choose a redshift bin width that is as small as possible, given the practical constraints imposed by redshift resolution and especially by numerical computation. In order to extract all the information, we need to include cross-correlations between bins – and this becomes numerically prohibitive for very large numbers of bins. To tackle this problem, we follow the 'hybrid' method proposed in [27] – i.e., we divide the full redshift range of a survey into sub-surveys and perform all cross-bin correlations in each sub-survey, but not between sub-survey bins. There is a small loss of information from neglecting some cross-correlations between redshift bins. However, if the sub-surveys are wide enough, i.e., bigger than the correlation length (which is typically ~ 0.1 in redshift), this loss is only non-negligible for adjacent bins of sub-surveys [27]. We use a redshift bin-width of $\Delta z = 0.01$, which is numerically feasible with the hybrid method.

In the hybrid approach, the constraints from a survey are just the summed constraints from each sub-survey. We modify this slightly in order to deal with the survey-dependence of the clustering bias. We marginalise over the bias parameters $b(z_i)$ in the Fisher matrices for each sub-survey, before adding these matrices to obtain the Fisher matrix of the full survey. In more detail: let $^I\tilde{F}_{\varphi_\alpha\varphi_\beta}$ be the Fisher matrix of sub-survey I marginalised over the clustering bias, so that φ_α are all the parameters in (2.18) except for $b^I(z_i)$. Then

$$^I\tilde{F}_{\varphi_\alpha\varphi_\beta} = \left[\left(^I F_{\vartheta_\alpha\vartheta_\beta} \right)^{-1}_{\varphi_\alpha\varphi_\beta} \right]^{-1} , \tag{4.1}$$

and the total Fisher matrix is

$$\tilde{F}_{\varphi_\alpha \varphi_\beta} = \sum_I {}^I \tilde{F}_{\varphi_\alpha \varphi_\beta} \,. \tag{4.2}$$

In the case of the low-redshift surveys BGS, SKA1 IM2, SKA1 Gal, and MK IM-L, the number of bins is low enough compute the full tomographic result. We compared this with the result from the sub-survey approximation with 2 sub-surveys, and found that the sub-survey approximation is only slightly worse, at the second significant figure.

4.2 Forecast results

We summarise the errors on γ in Table 4. The best forecasts (including Planck 2018 priors) are in the range $\sim 3 - 5\%$ for the near-future surveys. This is only improved to percent level in the more futuristic HI galaxy survey with SKA2. In Figure 4 we show the contour plots for γ and the total matter density today, $\Omega_{m0} = \Omega_{cdm0} + \Omega_{b0}$.

Table 4. Errors on γ in spectroscopic surveys, with and without Planck 2018 priors. Note that the last sub-survey may have a different number of bins as it is just the remainder.

Redshift	Survey	Subsurveys		$\sigma_{\ln\gamma}^{cond}$	$\sigma_{\ln\gamma}$	
		#	# bins each		no prior	with prior
				%	%	%
Low redshift	BGS	1	50	2.6	6.7	4.5
	SKA1 Gal	1	48	3.6	14.0	6.4
	MK IM-L	1	48	2.9	10.8	5.7
	SKA1 IM2	1	48	1.2	4.6	2.8
High redshift	Hα Spectr	3	45	1.4	3.9	2.9
	MK IM-U	2	52	2.9	17.8	8.0
	SKA1 IM1	5	45	1.2	5.3	3.7
Low and high	SKA2 Gal	4	47	0.6	1.7	1.4

5 Conclusions

In this paper, we computed constraints on the growth index γ using the observed power spectrum, i.e. the angular power spectrum C_ℓ, of spectroscopic cosmological surveys. Instead of an exhaustive study of surveys, we tried to fill the redshift range $0 < z \lesssim 3$ with the potentially best contemporaneous spectroscopic surveys. We first investigated the effect of redshift bin width on the amount of information on γ that can be extracted. Unlike the case of the Fourier power spectrum P_g, the choice of redshift bin width has a significant impact in the angular power spectrum. We showed that cross-correlations between bins compensates for the growth in noise, and we concluded that in theory, the thinnest possible width will deliver the highest signal-to-noise. Numerical constraints from the high number of cross-correlations between redshift bins can be mitigated by a 'hybrid' method, and we chose a bin width of $\Delta z = 0.01$.

Key advantages of C_ℓ include: it incorporates the redshift evolution of all cosmological, astrophysical and noise variables; it does not impose a flat-sky approximation but naturally incorporates wide-angle correlations; Doppler and lensing corrections to the 2-point correlations are also naturally included. Furthermore, since it is directly observable, the angular
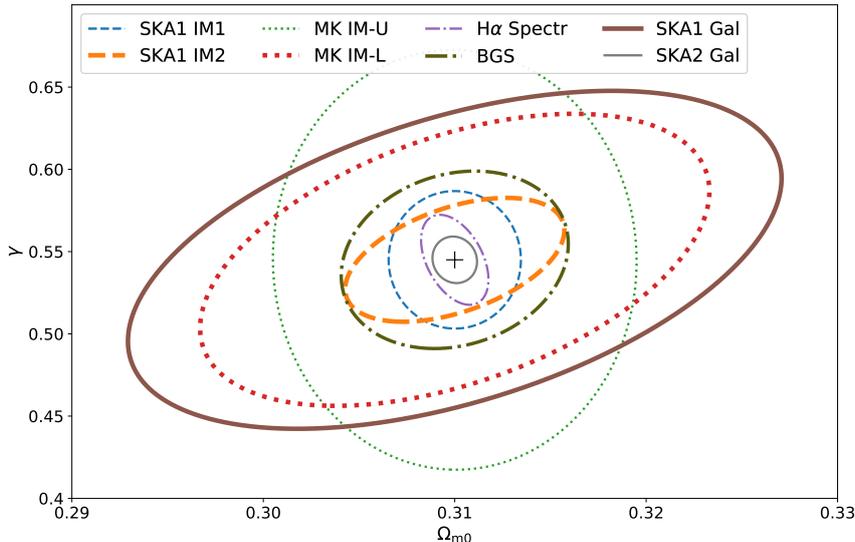
Figure 4. Marginal 1σ contour plots of γ and Ω_{m0} for the surveys considered. Plus sign indicates the fiducial values. No priors included.

Table 5. As in Table 4, but *neglecting* all cross-bin correlations

Redshift	Survey	$\sigma_{\ln\gamma}^{\mathrm{cond}}$	$\sigma_{\ln\gamma}$	
			no prior	with prior
		%	%	%
Low redshift	BGS	3.6	26.1	8.4
	SKA1 Gal	4.4	62.0	9.8
	MK IM-L	3.3	65.2	9.1
	SKA1 IM2	1.4	27.4	5.1
High redshift	Hα Spectr	1.7	14.6	7.2
	MK IM-U	3.2	124.2	11.0
	SKA1 IM1	1.3	26.7	6.4
Low and high	SKA2 Gal	0.7	4.9	3.4

power spectrum of the data requires no fiducial model and therefore no Alcock-Paczynski correction is needed.

These advantages over the Fourier power spectrum P_g (which is not an observable) come with a price. Unlike P_g, C_ℓ does not allow a clean separation of the RSD effect. In addition, there are computational challenges in extracting maximal information from C_ℓ. In particular, performing all cross-bin correlations becomes increasingly difficult for the very thin bins. We used a variant of a 'hybrid' method to capture the dominant cross-correlation contribution. Including cross-bin contributions is very important. In Table 5 we show the constraints computed when neglecting all cross-bin correlations and using only auto-correlations. By comparing with Table 4, we see that the marginal constraints with priors are degraded by a factor of $\sim 40-150\%$, and those without priors are degraded by much more.

In our Fisher forecasts, we marginalised over the standard cosmological parameters, as well as the dark energy equation of state and the clustering bias in each redshift bin, for each survey. Our constraints are based only on the information from linear scales. Our main results are shown in Table 4 and in the error contour plots of Figure 4. The best marginal constraints (including priors) on γ are $\sim 3-5\%$ for the near-future surveys, with SKA1 intensity mapping providing the best near-future constraints, while the SKA precursor MeerKAT is predicted to be competitive. The more futuristic SKA2 HI galaxy survey should reach sub-percent errors.

Acknowledgments

A SKA1 intensity mapping noise

We need to weight the noise and beam from the 64 MeerKAT dishes and the 133 new dishes, with different diameters and receiver bands (see Table 1). We weight the contributions of the different antennas using the individual RMS. For the UHF/L-bands and Band 1/2 we have:

$$w_{\mathrm{U/L}} = w_{\mathrm{tot}}^{-1} \, \frac{N_{\mathrm{d,U/L}}}{T_{\mathrm{sys,U/L}}^2} \,, \quad w_{1/2} = w_{\mathrm{tot}}^{-1} \, \frac{N_{d,1/2}}{T_{\mathrm{sys},1/2}^2} \,, \tag{A.1}$$

where

$$w_{\mathrm{tot}} = \frac{N_{\mathrm{d,U/L}}}{T_{\mathrm{sys,U/L}}^2} + \frac{N_{\mathrm{d},1/2}}{T_{\mathrm{sys},1/2}^2} \,. \tag{A.2}$$

Then the weighted instrumental noise for SKA1 surveys is given by

$$\mathcal{T}_\ell^{\mathrm{SKA1\,IM1/2}} = w_{\mathrm{U/L}} \mathcal{T}_\ell^{\mathrm{U/L}} + w_{1/2} \mathcal{T}_\ell^{1/2} = \frac{2\pi \, f_{\mathrm{sky}}}{\Delta\nu \, t_{\mathrm{tot}}} \frac{T_{\mathrm{sys,eff}}^2}{N_{\mathrm{d,tot}}} \,, \tag{A.3}$$

where $\mathcal{T}_\ell^{\mathrm{U/L}}$ is the noise for 64 MeerKAT dishes in UHF/L-bands, and $\mathcal{T}_\ell^{\mathrm{U1/2}}$ is the noises for 133 new SKA dishes in Bands 1/2 – each given by (3.4).

The system temperatures, in the form T^2/N, are shown in Figure 5, for the individual receivers (left) and for SKA1 using the weighted noise (A.3) (right). For the MeerKAT bands the system temperature and the effective one are the same. Note that the jumps in the effective system temperature for SKA1 IM1/2 arise from the fact that the frequency range of the SKA1 bands and the MeerKAT bands do not perfectly overlap.

Finally, the total weighted beam is simply given by

$$B_\ell^{\mathrm{SKA1\,IM1/2}} = w_{1/2} B_\ell^{1/2} + w_{\mathrm{U/L}} B_\ell^{\mathrm{U/L}} \,. \tag{A.4}$$
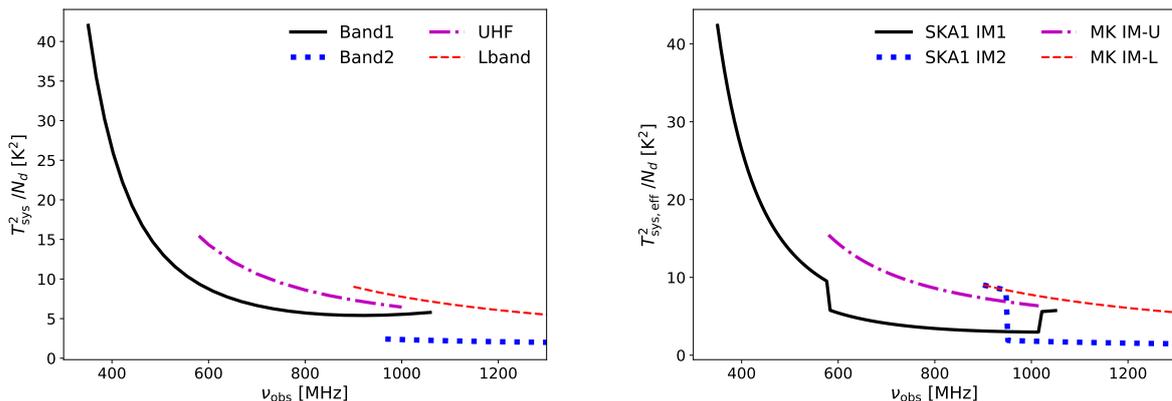

Figure 5. System temperature (in the form T^2/N) for the 4 receiver bands of HI IM (*left*) and the weighted effective system temperature for SKA1 and MeerKAT (*right*).

References

[1] T. Clifton, P. G. Ferreira, A. Padilla and C. Skordis, *Modified Gravity and Cosmology*, *Phys. Rept.* **513** (2012) 1 [1106.2476].

[2] K. Koyama, *Cosmological Tests of Modified Gravity*, *Rept. Prog. Phys.* **79** (2016) 046902 [1504.04623].

[3] D. Langlois, *Dark energy and modified gravity in degenerate higher-order scalar–tensor (DHOST) theories: A review*, *Int. J. Mod. Phys.* **D28** (2019) 1942006 [1811.06271].

[4] EUCLID COLLABORATION collaboration, *Euclid Definition Study Report*, *ESA-SRE* **12** (2011) [1110.3193].

[5] CHIME Collaboration, "CHIME Overview." http://chime.phas.ubc.ca/CHIME_overview.pdf, 2012.

[6] X. Chen, *The Tianlai Project: a 21CM Cosmology Experiment*, *International Journal of Modern Physics Conference Series* **12** (2012) 256 [1212.6278].

[7] R. A. Battye, M. L. Brown, I. W. A. Browne, R. J. Davis, P. Dewdney, C. Dickinson et al., *BINGO: a single dish approach to 21cm intensity mapping*, 1209.1041.

[8] DESI collaboration, *The DESI Experiment, a whitepaper for Snowmass 2013*, 1308.0847.

[9] O. Doré et al., *Cosmology with the SPHEREX All-Sky Spectral Survey*, 1412.4872.

[10] L. B. Newburgh et al., *HIRAX: A Probe of Dark Energy and Radio Transients*, *Proc. SPIE Int. Soc. Opt. Eng.* **9906** (2016) 99065X [1607.02059].

[11] M. G. Santos, M. Cluver, M. Hilton, M. Jarvis, G. I. G. Jozsa, L. Leeuw et al., *MeerKLASS: MeerKAT Large Area Synoptic Survey*, 1709.06099.

[12] SKA collaboration, *Cosmology with Phase 1 of the Square Kilometre Array: Red Book 2018: Technical specifications and performance forecasts*, *Submitted to: Publ. Astron. Soc. Austral.* (2018) [1811.02743].

[13] G.-B. Zhao et al., *The clustering of the SDSS-IV extended Baryon Oscillation Spectroscopic Survey DR14 quasar sample: a tomographic measurement of cosmic structure growth and expansion rate based on optimal redshift weights*, *Mon. Not. Roy. Astron. Soc.* **482** (2019) 3497 [1801.03043].

[14] P. Bull, *Extending cosmological tests of General Relativity with the Square Kilometre Array*, *Astrophys. J.* **817** (2016) 26 [1509.07562].

[15] L. Amendola et al., *Cosmology and fundamental physics with the Euclid satellite*, *Living Rev. Rel.* **21** (2018) 2 [1606.00180].

[16] A. Pourtsidou, D. Bacon and R. Crittenden, *HI and cosmological constraints from intensity mapping, optical and CMB surveys*, *Mon. Not. Roy. Astron. Soc.* **470** (2017) 4251 [1610.04189].

[17] R. Ruggeri, W. J. Percival, E.-M. Mueller, H. Gil-Marin, F. Zhu, N. Padmanabhan et al., *The extended Baryon Oscillation Spectroscopic Survey: testing a new approach to measure the evolution of the structure growth*, *Mon. Not. Roy. Astron. Soc.* **484** (2019) 4100 [1712.03997].

[18] A. Challinor and A. Lewis, *The linear power spectrum of observed source number counts*, *Phys. Rev.* **D84** (2011) 043516 [1105.5292].

[19] C. Bonvin and R. Durrer, *What galaxy surveys really measure*, *Phys. Rev.* **D84** (2011) 063505 [1105.5280].

[20] M. Bruni, R. Crittenden, K. Koyama, R. Maartens, C. Pitrou and D. Wands, *Disentangling non-Gaussianity, bias and GR effects in the galaxy distribution*, *Phys. Rev.* **D85** (2012) 041301 [1106.3999].

[21] E. Di Dio, F. Montanari, R. Durrer and J. Lesgourgues, *Cosmological Parameter Estimation with Large Scale Structure Observations*, *JCAP* **1401** (2014) 042 [1308.6186].

[22] V. Tansella, C. Bonvin, R. Durrer, B. Ghosh and E. Sellentin, *The full-sky relativistic correlation function and power spectrum of galaxy number counts. Part I: theoretical aspects*, *JCAP* **1803** (2018) 019 [1708.00492].

[23] J. Asorey, M. Crocce, E. Gaztanaga and A. Lewis, *Recovering 3D clustering information with angular correlations*, *Mon. Not. Roy. Astron. Soc.* **427** (2012) 1891 [1207.6487].

[24] J. E. Campagne, J. Neveu and S. Plaszczynski, *Angpow: a software for the fast computation of accurate tomographic power spectra*, *Astron. Astrophys.* **602** (2017) A72 [1701.03592].

[25] V. Assassi, M. Simonovi and M. Zaldarriaga, *Efficient evaluation of angular power spectra and bispectra*, *JCAP* **1711** (2017) 054 [1705.05022].

[26] H. S. Grasshorn Gebhardt and D. Jeong, *Fast and accurate computation of projected two-point functions*, *Phys. Rev.* **D97** (2018) 023504 [1709.02401].

[27] S. Camera, J. Fonseca, R. Maartens and M. G. Santos, *Optimized angular power spectra for spectroscopic galaxy surveys*, *Mon. Not. Roy. Astron. Soc.* **481** (2018) 1251 [1803.10773].

[28] N. Schneberg, M. Simonovi, J. Lesgourgues and M. Zaldarriaga, *Beyond the traditional Line-of-Sight approach of cosmological angular statistics*, *JCAP* **1810** (2018) 047 [1807.09540].

[29] A. Loureiro et al., *ZXCorr: Cosmological Measurements from Angular Power Spectra Analysis of BOSS DR12 Tomography*, *Mon. Not. Roy. Astron. Soc.* **485** (2019) 326 [1809.07204].

[30] LSST DARK ENERGY SCIENCE collaboration, *A unified pseudo-C_ℓ framework*, *Mon. Not. Roy. Astron. Soc.* **484** (2019) 4127 [1809.09603].

[31] K. Tanidis and S. Camera, *Developing a unified pipeline for large-scale structure data analysis with angular power spectra - I. The importance of redshift-space distortions for galaxy number counts*, 1902.07226.

[32] D. Jeong, F. Schmidt and C. M. Hirata, *Large-scale clustering of galaxies in general relativity*, *Phys. Rev.* **D85** (2012) 023504 [1107.5427].

[33] A. Hall, C. Bonvin and A. Challinor, *Testing General Relativity with 21-cm intensity mapping*, *Phys. Rev.* **D87** (2013) 064026 [1212.0728].

[34] M. Tegmark, A. Taylor and A. Heavens, *Karhunen-Loeve eigenvalue problems in cosmology: How should we tackle large data sets?*, *Astrophys. J.* **480** (1997) 22 [astro-ph/9603021].

[35] A. Witzemann, D. Alonso, J. Fonseca and M. G. Santos, *Simulated multitracer analyses with HI intensity mapping*, *Mon. Not. Roy. Astron. Soc.* **485** (2019) 5519 [1808.03093].

[36] S. Cunnington, L. Wolz, A. Pourtsidou and D. Bacon, *Impact of Foregrounds on HI Intensity Mapping Cross-Correlations with Optical Surveys*, *Mon. Not. Roy. Astron. Soc.* **488** (2019) 5452 [1904.01479].

[37] PLANCK collaboration, *Planck 2018 results. VI. Cosmological parameters*, 1807.06209.

[38] J. Fonseca, R. Maartens and M. G. Santos, *Synergies between intensity maps of hydrogen lines*, *Mon. Not. Roy. Astron. Soc.* **479** (2018) 3490 [1803.07077].

[39] VIRGO CONSORTIUM collaboration, *Stable clustering, the halo model and nonlinear cosmological power spectra*, *Mon. Not. Roy. Astron. Soc.* **341** (2003) 1311 [astro-ph/0207664].

[40] Z.-M. Ma, W. Hu and D. Huterer, *Effect of photometric redshift uncertainties on weak lensing tomography*, *Astrophys. J.* **636** (2005) 21 [astro-ph/0506614].

[41] L. Knox, *Determination of inflationary observables by cosmic microwave background anisotropy experiments*, *Phys. Rev.* **D52** (1995) 4307 [astro-ph/9504054].

[42] M. Santos, P. Bull, D. Alonso, S. Camera, P. Ferreira, G. Bernardi et al., *Cosmology from a SKA HI intensity mapping survey*, in *Advancing Astrophysics with the Square Kilometre Array (AASKA14)*, p. 19, Apr, 2015, 1501.03989.

[43] J. Fonseca, S. Camera, M. Santos and R. Maartens, *Hunting down horizon-scale effects with multi-wavelength surveys*, *Astrophys. J.* **812** (2015) L22 [1507.04605].

[44] S. Yahya, P. Bull, M. G. Santos, M. Silva, R. Maartens, P. Okouma et al., *Cosmological performance of SKA HI galaxy surveys*, *Mon. Not. Roy. Astron. Soc.* **450** (2015) 2251 [1412.4700].

[45] S. Camera, M. G. Santos and R. Maartens, *Probing primordial non-Gaussianity with SKA galaxy redshift surveys: a fully relativistic analysis*, *Mon. Not. Roy. Astron. Soc.* **448** (2015c) 1035 [1409.8286].

[46] M. Santos, D. Alonso, P. Bull, M. B. Silva and S. Yahya, *HI galaxy simulations for the SKA: number counts and bias*, in *Advancing Astrophysics with the Square Kilometre Array (AASKA14)*, p. 21, Apr, 2015, 1501.03990.

[47] L. Pozzetti, C. M. Hirata, J. E. Geach, A. Cimatti, C. Baugh, O. Cucciati et al., *Modelling the number density of Hα emitters for future spectroscopic near-IR space missions*, *Astron. Astrophys.* **590** (2016) A3 [1603.01453].

[48] Euclid Theory Working Group collaboration, *Cosmology and fundamental physics with the Euclid satellite*, *Living Rev. Rel.* **16** (2013) 6 [1206.1225].

[49] DESI collaboration, *The DESI Experiment Part I: Science,Targeting, and Survey Design*, 1611.00036.